Ground Testing of Spacecraft Attitude Dynamics during In-Space Assembly and Manufacturing

Harsh G. Bhundiya*, Zachary C. Cordero†
Massachusetts Institute of Technology, Cambridge, MA, USA

Michael A. Marshall ‡
The Johns Hopkins University Applied Physics Laboratory, Laurel, MD, USA

David Sternberg §, Kevin Lo ¶, and Swati Mohan ‖
Jet Propulsion Laboratory, California Institute of Technology, Pasadena, CA, USA

The on-orbit construction of structures, i.e., in-space assembly and manufacturing (ISAM), is a promising approach for increasing mission flexibility and achieving structures optimized for the space environment. Although many construction processes have been proposed, a critical aspect that needs further investigation is the spacecraft attitude dynamics during ISAM given the large changes in mass properties of the spacecraft and the long timescales of fabrication. This work investigates the ground testing of spacecraft attitude dynamics during Bend-Forming, a candidate process for the on-orbit construction of truss structures via plastic deformation of metallic feedstock. Specifically, we conduct experiments on a planar air bearing platform and develop rigid body dynamics models to understand the platform motion during Bend-Forming. The experimental results reveal 1) the effect of metal springback on the attitude dynamics, and 2) the possibility of control-structure interaction during fabrication with closed-loop, thruster-based position and attitude control. Overall, this study highlights how artifacts of the manufacturing process like springback affect attitude dynamics and results in important guidelines for the ground testing of spacecraft attitude dynamics during ISAM.

I. Introduction

In-space assembly and manufacturing (ISAM) refers to the on-orbit construction of structures from pre-fabricated components or raw feedstock materials and offers a promising approach for increasing mission flexibility and achieving structures optimized for the space environment. ISAM has been of interest for decades, but most research and development to date has focused on ground-based or microgravity-based demonstrations of candidate construction processes. For example, recent concepts include the construction of support structures for large space telescopes [1–3], the assembly of truss bays to form a perimeter truss for a large mesh reflector antenna [4], and the extrusion of both UV photopolymer feedstocks [5] and fiber-reinforced composites [6, 7] to fabricate truss support structures. Another concept called Bend-Forming [8], developed by the authors, forms truss structures via computer numerical control (CNC) deformation processing of metallic feedstock.

Each construction process is intended to fabricate large structures on orbit, but important aspects that have not been fully investigated are the attitude dynamics during and attitude control system (ACS) design for ISAM. The construction process causes relative motion of pre-fabricated components or feedstock material within the spacecraft, inducing internal forces and torques that affect the spacecraft orientation. For long-duration ISAM missions with large mass properties changes, passive attitude control may be insufficient for maintaining the spacecraft orientation. In these scenarios, typical strategies such as idling the ACS and subsequently recovering the orientation, as was done, for example, during the deployments of the solar panels on the Psyche mission [9] and the solar sail on the ACS3

---

*Ph.D. Candidate, Department of Aeronautics and Astronautics, bhundiya@mit.edu, AIAA Student Member
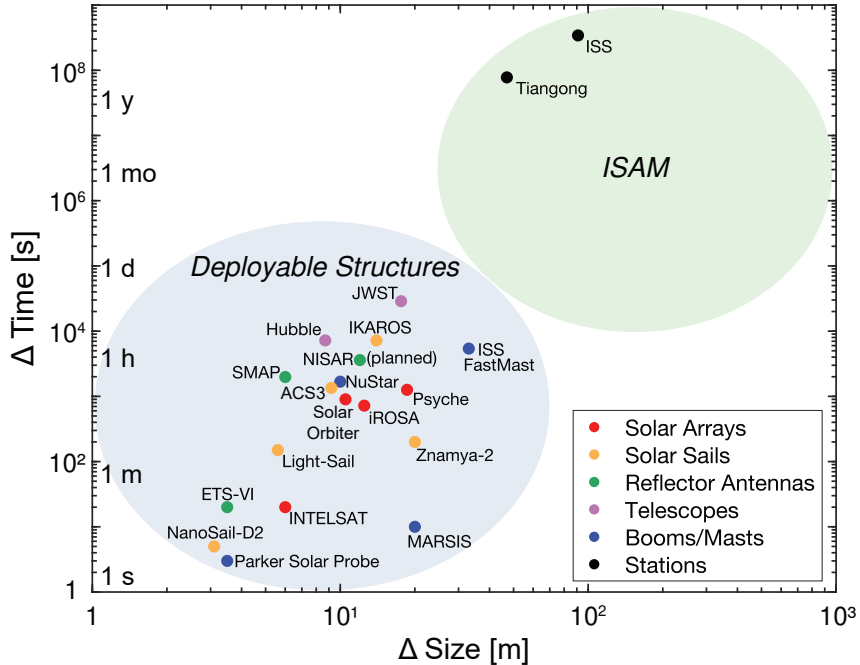
†Edgerton Career Development Professor, Department of Aeronautics and Astronautics, zcordero@mit.edu, AIAA Member

‡Guidance and Control Analyst, Space Exploration Sector, michael.a.marshall@jhuapl.edu, AIAA Member

§Guidance and Control Engineer, Payload/Instrument Pointing Control Systems Engineering Group, david.c.sternberg@jpl.nasa.gov, AIAA Senior Member

¶Guidance and Control Engineer, GNC Hardware and Testbed Development Group, kevin.d.lo@jpl.nasa.gov

‖Guidance and Control Engineer, GNC Technical Staff, swati.mohan@jpl.nasa.gov

Fig. 1   Comparison of size and timescale of in-space assembly and manufacturing (ISAM) versus deployable structures. Modern deployable structures achieve dimensions of tens of meters after a time period of seconds to hours. ISAM enables larger structures but requires construction over longer time periods.

mission [10], may be insufficient for long-duration ISAM missions. Figure 1 illustrates this point with a comparison of size and timescale of deployable structures versus future ISAM technologies. Whereas deployable structures achieve dimensions of tens of meters after a time period of seconds to hours, ISAM may enable larger structures over a longer time period of days to months. Over such long timescales, external disturbances torques will significantly affect the spacecraft orientation, motivating the need for active attitude control. At the same time, using active attitude control to maintain a fixed spacecraft orientation during the entire construction process poses severe constraints on the fabrication time of large structures, as demonstrated by our analysis in Ref. [11]. To develop an effective attitude control strategy for ISAM spacecraft, it is essential to understand the attitude dynamics during the construction process.

Some recent work has begun to investigate the spacecraft attitude dynamics during ISAM, primarily through numerical modeling. One study [12] has presented the dynamics and control of a free-flying spacecraft with a robotic manipulator for applications such as additive manufacturing. This study used rigid body dynamics to model the relative spacecraft motion and control inputs to maintain orientation during the fabrication process. Other studies [13–15] have focused on the design of attitude controllers during the autonomous assembly of modules for applications like large space telescopes. These studies have developed control laws to manage the large changes in mass properties during construction and validated them through rigid and flexible body dynamics models. Whereas these previous studies have primarily focused on numerical models, experimental validation is scarce, with only one study [16] investigating the fused filament fabrication of truss structures with a robotic arm on an air bearing platform. This work used a proportional-integral-derivative (PID) controller to keep the robot arm steady; however, there was no analysis of the spacecraft attitude dynamics during fabrication.

The ground testing of attitude dynamics is particularly important for developing robust ACSs for future ISAM spacecraft. Ground testing can provide insights into how artifacts of the specific ISAM process affect the dynamics, validate whether numerical models capture the essential physics, and test specific attitude control algorithms and technologies. Various methods exist for the ground testing of spacecraft attitude dynamics with different levels of complexity and degrees of freedom (DOF): robotic arm systems, planar air bearing platforms, spherical air bearing platforms, and a combination of planar and spherical air bearing platforms (see Refs. [17, 18] for a summary). Similar methods are also used for the ground testing of deployable structures [19–21], for which air bearing platforms are often combined with gravity offloading to replicate the motion during deployment. These systems provide a method

2

of approximating the motion in a nearly frictionless environment with 3 to 6-DOF. Historically, planar air bearing platforms that translate and rotate on a flat floor (i.e., 3-DOF) have been a popular choice for ground testing of attitude dynamics, and results from ground tests have also been validated with spacecraft flight data [22]. For these reasons, air bearing platforms offer a promising avenue for the ground testing of spacecraft attitude dynamics during ISAM. The simplicity of air bearing platforms also makes them well-suited for integration with ISAM processes.

The present work investigates spacecraft attitude dynamics during Bend-Forming [8], a candidate process for manufacturing truss structures via deformation processing of metallic feedstock, through experiments on an air bearing platform. In particular, a CNC wire bender is integrated with an active, planar air bearing platform (Sec. II), and experiments are conducted with both free-floating motion and closed-loop, thruster-based position and attitude control of the platform. To understand the essential physics of the spacecraft motion during Bend-Forming, the experiments consider the unit fabrication steps of extrusion and plastic deformation, as well as the fabrication of a larger geometry with multiple unit fabrication steps. The experimental results (Sec. III) are compared against a rigid body dynamics model which considers the changes in mass properties of the platform, providing insights (Sec. IV) into the important physics and challenges to attitude control during Bend-Forming. Lastly, a conclusion and outlook (Sec. V) discuss important considerations for ground testing of spacecraft attitude dynamics during ISAM.

II. Experimental and Modeling Setup

A. Guidance, Navigation, Control and Spacecraft Autonomy Testbed (GSAT)

The present experiments were conducted at the Guidance, Navigation, Control and Spacecraft Autonomy Testbed (GSAT), formerly known as the Small Satellite Dynamics Testbed (SSDT), at the NASA Jet Propulsion Laboratory [18, 22, 23]. This facility houses a set of active air bearing platforms to test Guidance, Navigation, and Control (GNC) hardware and software on a large Teflon-coated floor. Each active air bearing platform consists of a compressed air system with two internal tanks of atmospheric air compressed to a maximum of 2400 psi. The air tanks feed compressed air to three porous carbon air bearings which create a thin layer of air ($< 70\ \mu$m) between the bearings and the testbed floor, allowing the platform to translate and rotate in a nearly frictionless environment. The air tanks also feed 90-psi compressed air to eight thrusters around the circumference, allowing the platform to maneuver on the testbed floor. To measure the platform motion, a Vicon motion capture system* is used to record position and rotation via reflective markers that yield an approximate translational resolution of 1 mm.

To understand the spacecraft attitude dynamics during Bend-Forming, a CNC wire bender from Pensa Labs[†] was integrated with the active air bearing platform, as depicted in Fig. 2. The mass properties of the experimental setup, listed in Table 1, were measured with a weighing scale and rotary table (KGR500[‡]). Here, the center of mass was measured from the origin labeled in Fig. 2, and the mass properties of the wire feedstock were estimated for a steel rod with constant density $\rho = 7800$ kg/m^3, diameter $d = 3.175$ mm (1/8"), and length $L = 1.8$ m. The CNC wire bender was configured to achieve a bending accuracy of approximately 1° after "springback", which refers to motion of the feedstock due to the release of residual stresses after plastic deformation [24]. A portable power station and headless computer were used to command the CNC wire bender via WiFi, eliminating the need for cables to the air bearing platform which would affect the dynamics. For the present experiments, a sequence of "feed" and "bend" steps, which respectively refer to the extrusion and localized plastic deformation of feedstock material, were commanded to the machine while the air bearing platform remained floating. The feed and bend steps represent the unit steps of the Bend-Forming process, as illustrated in Fig. 3. The experiments consisted of measuring the platform motion during these unit steps and the fabrication of a larger geometry with iterative feed and bend steps.

The experimental setup and test facility imposed several constraints on the types of structures and fabrication sequences that could be tested. First, the CNC wire bender could only fabricate 2D structures with feed and bend steps along the plane of the machine. 3D CNC wire bending machines[§] are available which rotate the wire out-of-plane, but these machines are larger and require a larger test facility than GSAT. Second, due to the lack of gravity offloading, only geometries with sufficient stiffness to not contact the testbed floor were fabricated. In practice, this meant limiting the total feed length to $L < 2$ m so that deflections due to gravity did not cause the feedstock to contact the testbed floor.

---

*https://www.vicon.com/hardware/cameras/

[†]https://www.pensalabs.com/

[‡]https://raptor-scientific.com/about-us/space-electronics/

[§]https://formingsystemsinc.com/3d-wire-forming-machines/
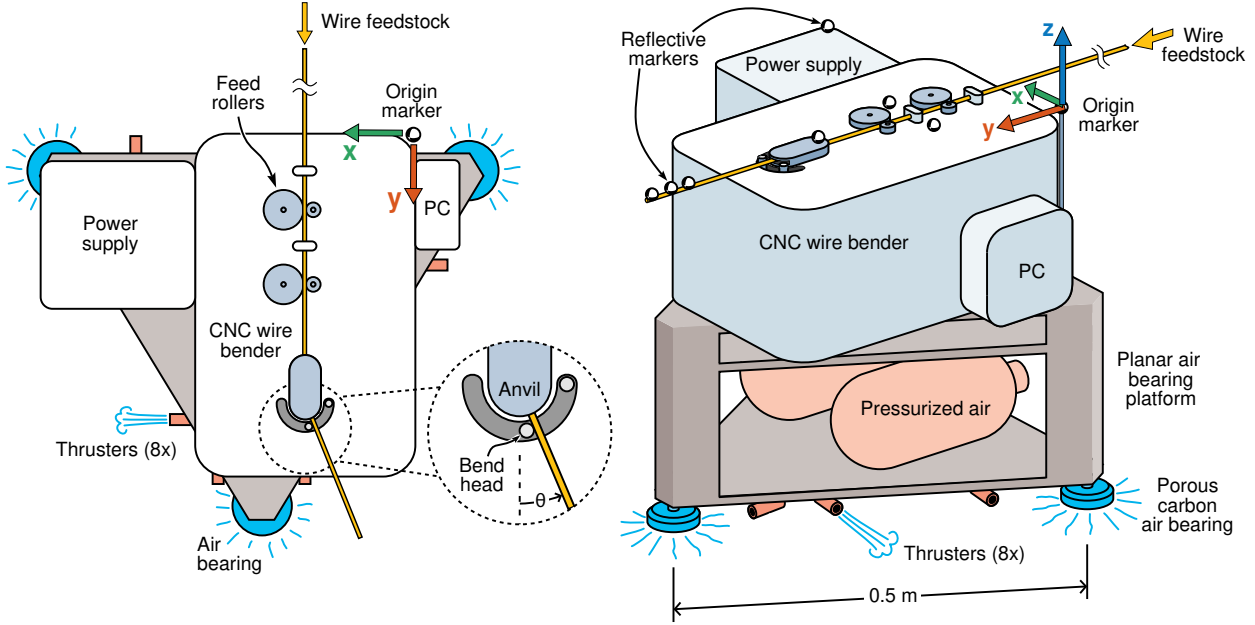
Fig. 2   Plan and oblique views of CNC wire bender integrated with planar air bearing platform used for ground testing of spacecraft attitude dynamics during Bend-Forming.

Table 1   Mass properties of experimental setup

Component	Mass, m [kg]	Center of Mass, x_{CM} [m]	Inertia, I_{CMzz} [kg m^2]
Wire feedstock	0.11	$[0.18, -0.38]^T$	0.032
Air bearing platform	14.9	$[0.21, 0.11]^T$	0.49
Air bearing platform with wire bender (no feedstock)	31.3	$[0.20, 0.12]^T$	0.93
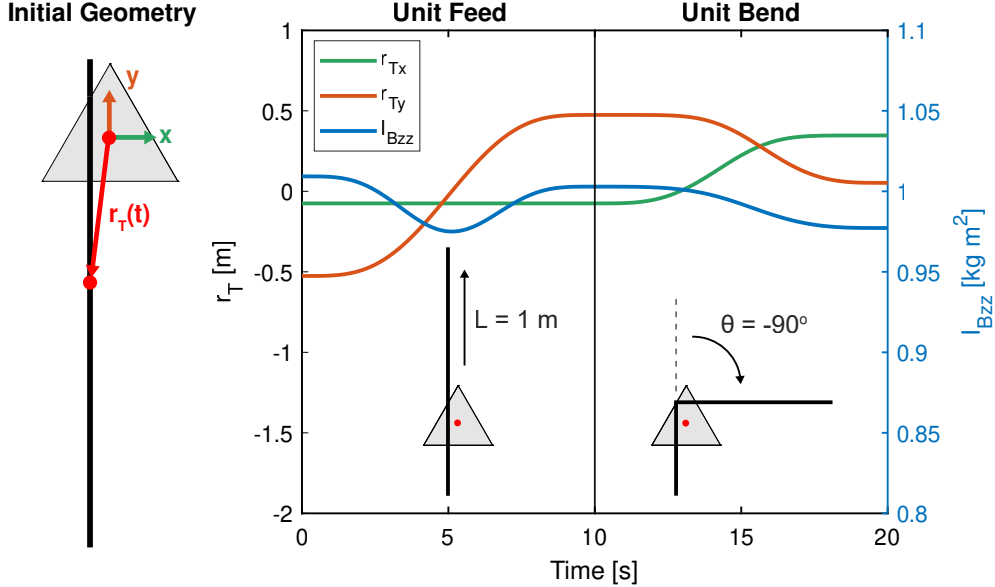
B. Variable-Geometry Rigid Body Dynamics Model

To understand the motion of the air bearing platform during Bend-Forming, a variable-geometry rigid body dynamics model is developed. Specifically, the air bearing platform and wire feedstock are modeled as rigid bodies within a control volume of constant mass and time-varying geometry. This approach models the changes in mass properties as internal forces and moments on the control volume, but does not model the flexibility of the slender feedstock or the deflections due to gravity. The force and moment equilibria for a variable-geometry rigid body are [25]:

$$\int_{CV} \rho \left(\ddot{\mathbf{R}} + \dot{\omega} \times \mathbf{r} + \omega \times \omega \times \mathbf{r} \right) \, dV + 2\omega \times \frac{\partial}{\partial t} \int_{CV} \rho \mathbf{r} \, dV + \frac{\partial^2}{\partial^2 t} \int_{CV} \rho \mathbf{r} \, dV = \mathbf{F}_{ext}, \tag{1}$$

$$\int_{CV} \rho \left(\mathbf{r} \times \ddot{\mathbf{R}} \right) \, dV + \mathbf{I}_B \dot{\omega} + \omega \times (\mathbf{I}_B \omega) + \dot{\mathbf{I}}_B \omega + \omega \times \int_{CV} \rho \left(\mathbf{r} \times \mathbf{v} \right) \, dV + \frac{\partial}{\partial t} \int_{CV} \rho \left(\mathbf{r} \times \mathbf{v} \right) \, dV = \mathbf{M}_{ext}, \tag{2}$$

where $\mathbf{R}$ is the inertial position of the body-fixed frame, ω and $\dot{\omega}$ are the angular velocity and acceleration of the body-fixed frame, $\mathbf{I}_B$ is the mass moment of inertia matrix about the body-fixed frame, $\mathbf{r}$ and $\mathbf{v}$ are the position and velocity of a point on the body relative to the body-fixed frame, and $\mathbf{F}_{ext}$ and $\mathbf{M}_{ext}$ are the external forces and moments. These equations model the rigid body dynamics with a body-fixed frame offset from the center of mass, and they allow for time-varying geometry within the control volume by specifying $\mathbf{r}(t)$, $\mathbf{v}(t)$, and $\mathbf{I}_B(t)$ as explicit functions of time

Fig. 3 Unit fabrication steps of Bend-Forming: unit feed L and unit bend θ. The specified motion of the feedstock ($\mathbf{r}_T$) and mass moment of inertia of the platform (I_{Bzz}) are inputs to the variable-geometry rigid body dynamics model.

(see Refs. [25, 26] for a complete description). If there is no time-varying geometry, i.e., $\mathbf{v}(t) = \mathbf{0}, \dot{\mathbf{I}}_B(t) = \mathbf{0}$, Eqs. (1) and (2) reduce to the classic Newton-Euler equations for rigid body dynamics.

To model the motion of the air bearing platform during Bend-Forming, we consider a control volume with two rigid bodies. One rigid body represents the air bearing platform centered at the body-fixed frame (i.e., $m_1 = m_{SC}, \mathbf{r}_1 = \mathbf{0}, \mathbf{v}_1 = \mathbf{0}, \mathbf{R} = \mathbf{x}_{SC}$), and the other represents the fabricated structure at its center of mass (i.e., $m_2 = m_T, \mathbf{r}_2 = \mathbf{r}_T, \mathbf{v}_2 = \mathbf{v}_T$). The total mass M remains constant (i.e., $M = m_1 + m_2$). We assume the motion is dominated by the changes in mass properties as the fabricated structure moves relative to the platform, with negligible effects from friction, air resistance, and other external forces and moments (i.e., $\mathbf{F}_{ext} = \mathbf{0}, \mathbf{M}_{ext} = \mathbf{0}$). Simplifying the integrals in Eqs. (1) and (2) and substituting these variables yields

$$M\ddot{\mathbf{x}}_{SC} + m_T (\dot{\boldsymbol{\omega}} \times \mathbf{r}_T + \boldsymbol{\omega} \times \boldsymbol{\omega} \times \mathbf{r}_T) + 2\boldsymbol{\omega} \times \frac{\partial}{\partial t}(m_T \mathbf{r}_T) + \frac{\partial^2}{\partial^2 t}(m_T \mathbf{r}_T) = \mathbf{0}, \tag{3}$$

$$m_T \mathbf{r}_T \times \ddot{\mathbf{x}}_{SC} + \mathbf{I}_B \dot{\boldsymbol{\omega}} + \boldsymbol{\omega} \times (\mathbf{I}_B \boldsymbol{\omega}) + \dot{\mathbf{I}}_B \boldsymbol{\omega} + \boldsymbol{\omega} \times (m_T \mathbf{r}_T \times \mathbf{v}_T) + \frac{\partial}{\partial t}(m_T \mathbf{r}_T \times \mathbf{v}_T) = \mathbf{0}. \tag{4}$$

In Eqs. (3) and (4), the changes in mass properties of the platform are specified as motion of the feedstock relative to the body-fixed frame ($\mathbf{r}_T, \mathbf{v}_T$) and the resulting changes in moment of inertia ($\mathbf{I}_B, \dot{\mathbf{I}}_B$). As an example, Fig. 3 shows the specified feedstock motion and inertia change during the unit feed and bend steps, assuming that the extrusion length and bend angle follow the smooth polynomial profile from Ref. [27] with zero velocity, acceleration, and jerk at the endpoints. Eqs. (3) and (4) are then numerically integrated using quaternion attitude kinematics [28] to yield the translational and rotational motion of the platform, and the method of Lagrange multipliers [29] is used to constrain the motion to the plane (i.e., $x_{SCz} = 0, \omega_x = \omega_y = 0$) in order to match the DOF in the experiment. Since Eqs. (3) and (4) do not include any external forces and moments, the resulting motion conserves linear and angular momentum, and the combined center of mass of the two rigid bodies remains stationary.
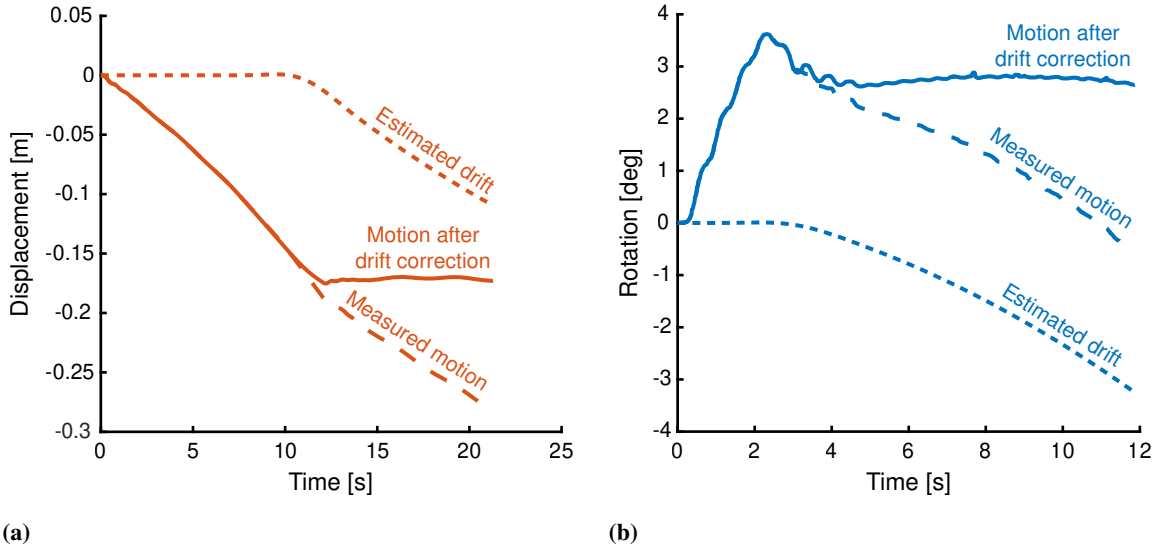
III. Results

Two sets of experiments were conducted on the air bearing platform to understand the spacecraft attitude dynamics during Bend-Forming. The first set of experiments (Sec. III.A) examined the free-floating platform motion during individual feed and bend steps, as well as during the fabrication of a zigzag geometry with multiple iterations of these steps. The zigzag geometry was chosen as a representative 2D structure that could be fabricated within the constraints

of the experimental setup and provide insights into how the motion changed with iterative fabrication steps. The second set of experiments (Sec. III.B) repeated the fabrication of the same geometries with closed-loop, thruster-based position and attitude control of the platform.

A. Free-Floating Motion

The free-floating experiments were conducted by floating the air bearing platform and measuring its motion due to different Bend-Forming fabrication sequences. The motion of the air bearing platform and the feedstock were measured using the Vicon motion capture system, with a total of seven reflective markers placed on the platform and at the wire tip (cf. Fig. 2). One challenge in getting accurate data with these experiments was the drift of the platform caused by imperfections of the testbed floor. As the air bearings provided an air cushion less than 70 μm thick between the platform and testbed floor, small imperfections such as seams, depressions, or dust on the floor affected the dynamics [22]. Additionally, the drift varied based on both the initial location of the platform and its motion during the experiment. Correcting for this drift was challenging for the free-floating experiments, especially for longer fabrication sequences with multiple steps, as it was difficult to determine when the drift began and how it varied during the experiment. However, for the unit feed and bend experiments, a drift correction procedure was implemented by assuming the drift began near the end of the fabrication step and computing a moving average of the subsequent motion, as depicted in Fig 4. This estimated drift was then subtracted from the measured motion, resulting in an expected plateau in displacement and rotation after completion of the fabrication step.


(a)

(b)

Fig. 4 (a) Translational and (b) rotational drift correction procedures during unit feed and unit bend steps.

Figure 5 shows snapshots of the predicted rigid-body motion during the free-floating experiments, and Fig. 6 plots the measured motion of the air bearing platform and the wire tip. For the first fabrication sequence of a unit feed, the wire was extruded to a length of $L = 0.5$ m at an approximate rate of 0.04 m/s. Given the small mass ratio between the wire feedstock and the air bearing platform with the wire bender (cf. Table 1), for this experiment the wire tip was attached to a secondary air bearing platform to increase the magnitude of the free-floating motion and provide gravity offloading. Following the coordinate frame in Fig. 2, the motion depicted in Fig. 6a shows the unit feed resulted in the platform displacing backwards ($-y$) and the wire tip displacing forwards ($+y$), with the final displacements approximately summing to the total feed length of $L = 0.5$ m. This relative motion is consistent with the rigid body dynamics model of Sec. II.B, which predicts displacement magnitudes equal to the feed length scaled by the respective masses of the platform and at the wire tip. Here, the discrepancies between model and experiment are due to differences between the simulated and actual feed profiles and the rigid connection between the wire tip and secondary air bearing platform assumed in the model.

For the second fabrication sequence of a unit bend, an initial wire length of $L_0 = 1$ m was plastically deformed to an angle of $\theta = -120°$ at a rate of $-60°$/s. The motion depicted in Fig. 6b shows that during the bend, the platform

rotated up to 4° counterclockwise (+z) while the wire rotated approximately 120° clockwise (−z). The rotation of the platform in the opposite direction as the wire is consistent with the conservation of angular momentum from the rigid body dynamics model, as depicted in Fig. 6b. However, the rigid body dynamics model does not capture the vibrations of the feedstock evident in the wire displacement, nor the decrease of approximately 1° in the platform rotation after completion of the unit bend at $t \approx 2$ s. This decrease in platform rotation resulted from the springback of the metal after plastic deformation, as discussed further in Sec. IV.

The third fabrication sequence consisted of a series of repeated unit feeds ($L = 0.06$ m) and unit bends ($\theta = \pm 90°$) which resulted in a zigzag geometry. The motion depicted in Fig. 6c shows that during this fabrication sequence, the platform displaced backwards (−y) and rotated counterclockwise (+z), while the wire displaced forwards (+y) and both right and left (±x) as a result of the positive and negative bend steps. The platform motion shows how each iteration of the feed and bend steps increased the total displacement and rotation. The downward displacement of the wire tip (-z) also shows the increasing effect of gravity as the cantilever length from the platform to the wire tip increased. Here we see the rigid body model accurately predicts the motion of the platform and wire for roughly half the fabrication sequence ($t < 30$ s), but underestimates the motion for the remainder of the sequence. Additionally, the model does not capture the vibrations or springback of the wire feedstock, evident in Fig. 6c from the oscillations in wire displacement and sharp decreases in platform rotation after each bend step.

B. Motion with Thruster Control
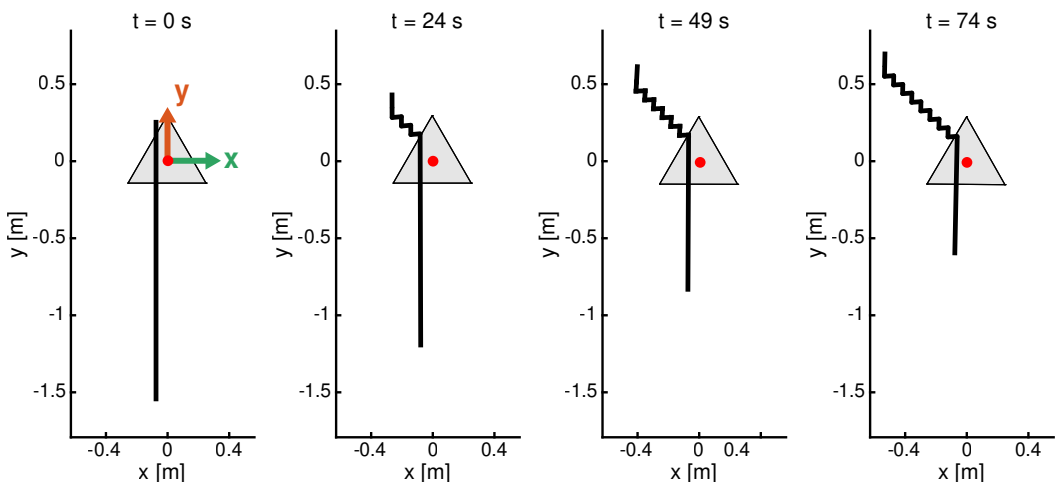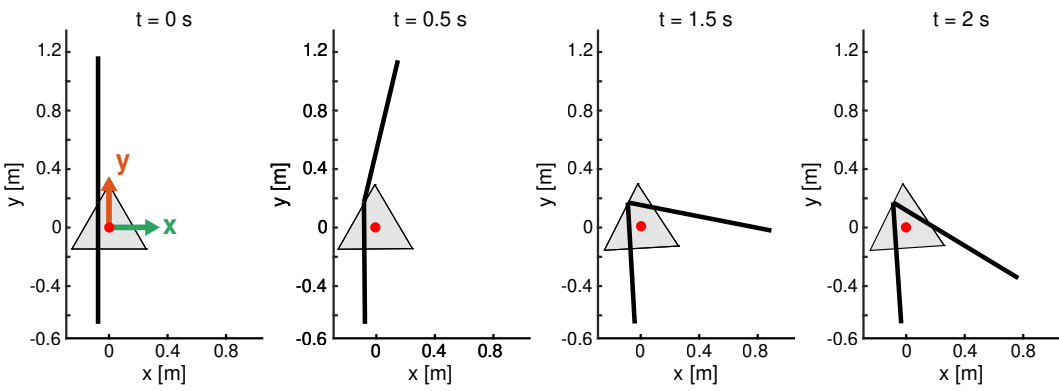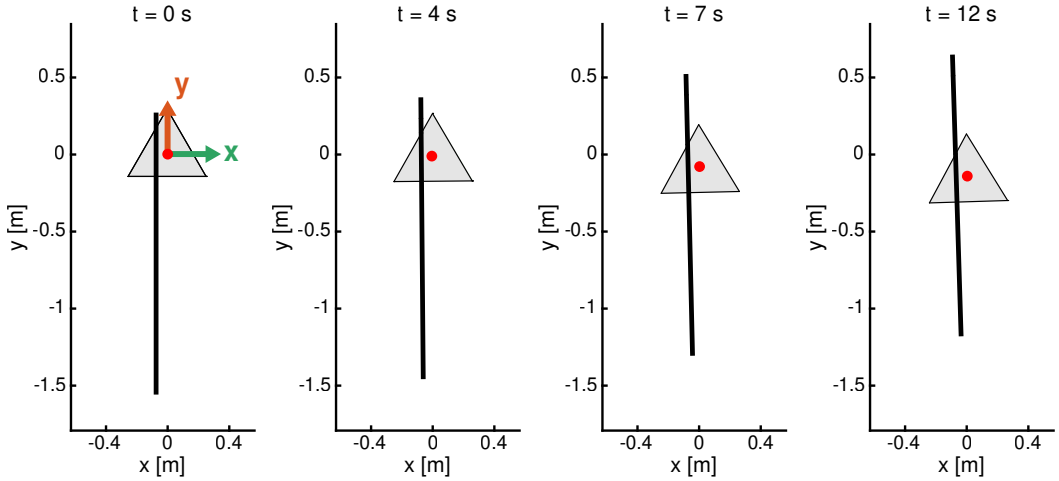
The second set of experiments implemented the same fabrication sequences as Sec. III.A, but with closed-loop, thruster-based attitude and position control of the platform. To this end, the hardware setup described in Refs. [18, 23] was used to control the eight thrusters around the circumference of the air bearing platform (cf. Fig. 2). The thruster control was implemented by using the motion captured by the Vicon system as the positional and rotational error for a proportional-derivative (PD) controller with a closed-loop bandwidth of approximately 5 Hz. The PD controller computed the forces and torques to apply, which were converted to thrust durations between 10-200 ms for each thruster.

Figure 7 plots the measured motion of the air bearing platform and the commanded thruster forces and torques during the unit feed, the unit bend, and fabrication of the zigzag geometry with position and attitude control. Compared to the free-floating experiments, the unit feed was implemented two times slower, and the fabrication of the zigzag geometry was three times slower. Additionally, for simplicity, fixed controller gains were used that were tuned to the mass properties of the air bearing platform without considering the wire feedstock. Fig. 7a shows that for the unit feed, the thruster control was sufficient in decreasing the platform displacement from around 20 cm in the free-floating experiment to less than 2 cm. For the unit bend, Fig. 7b shows that the thruster control only decreased the maximum platform rotation from 4° in the free-floating experiment to 2°, suggesting that the thrusters were not sufficient in maintaining a fixed orientation. This is also evident from the large undershoot in platform rotation at $t \approx 2$ s after completion of the bend step, which likely resulted from application of the thruster torque simultaneously as the springback of the wire. For the zigzag geometry, the platform motion in Fig. 7c shows that the thruster control was sufficient in maintaining the position and orientation for around half the fabrication sequence ($t < 70$ s), after which the error in displacement and rotation began to grow approximately linearly.
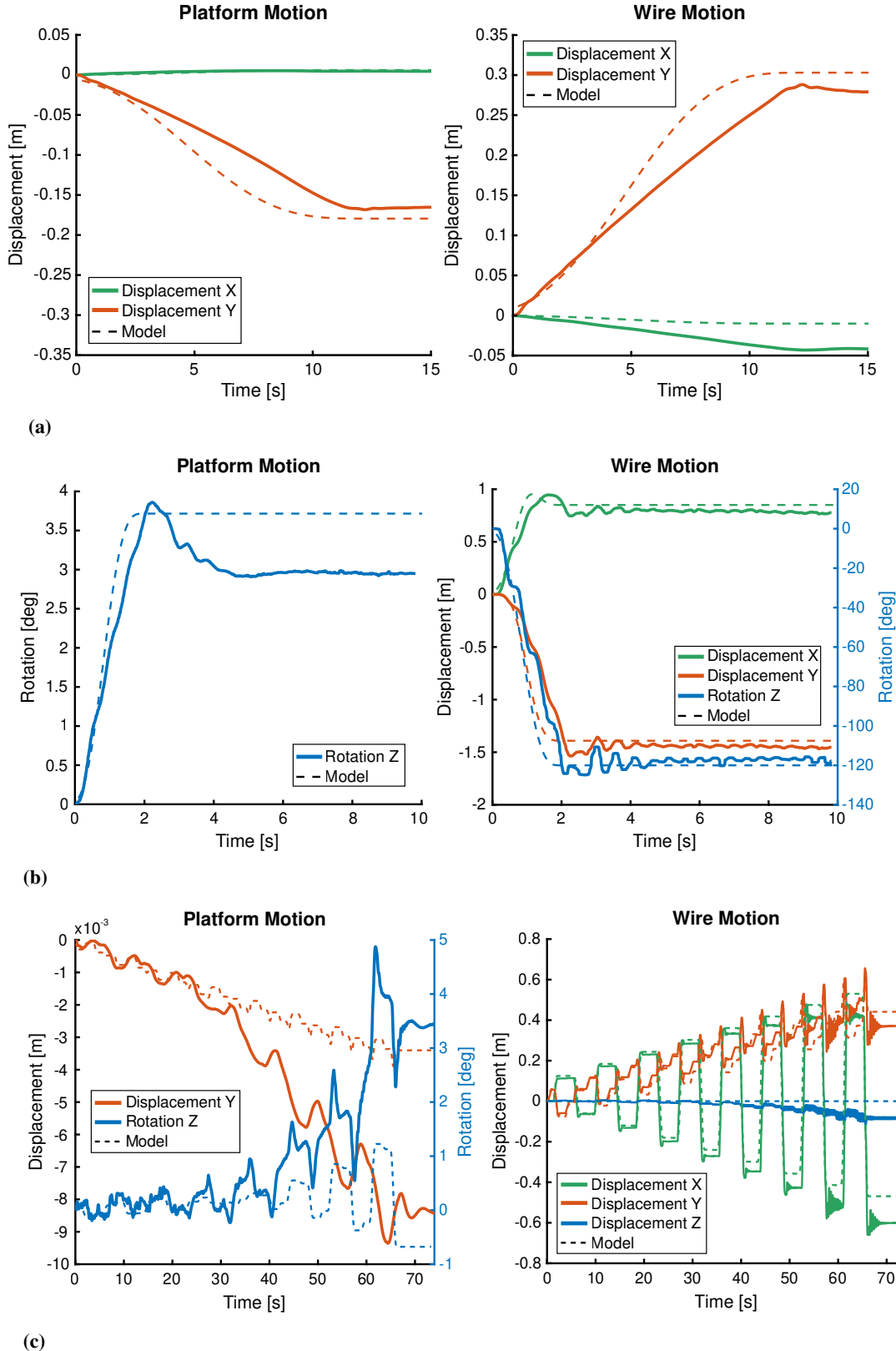
The plots of the commanded thruster forces and torques in Fig. 7 provide insights into the control requirements for maintaining the platform position and orientation during Bend-Forming. For both the unit feed and unit bend, the maximum thruster force and torque were measured at the beginning and end of the step, whereas for the zigzag geometry, the thruster force and torque increased during the fabrication sequence. The rigid body dynamics model of Sec. II.B provides estimates of the control force and torque that are consistent with these experimental results. Specifically by setting $\mathbf{x}_{SC} = 0$, $\boldsymbol{\omega} = 0$ in Eqs. (3) and (4), we find the control force and torque to maintain the position and orientation of the platform as $\mathbf{F}_C = \frac{\partial^2}{\partial^2 t}(m_T \mathbf{r}_T)$ and $\mathbf{T}_C = \frac{\partial}{\partial t}(m_T \mathbf{r}_T \times \mathbf{v}_T)$, respectively. The dashed lines in Fig. 7 plot the maximum values of the control force and torque during each fabrication sequence. These forces and torques underestimate the experimentally measured values but follow the same general trends. The underestimates are likely due to the additional control input required to counter platform drift and delays in the actual thruster application in the experiment.

IV. Discussion
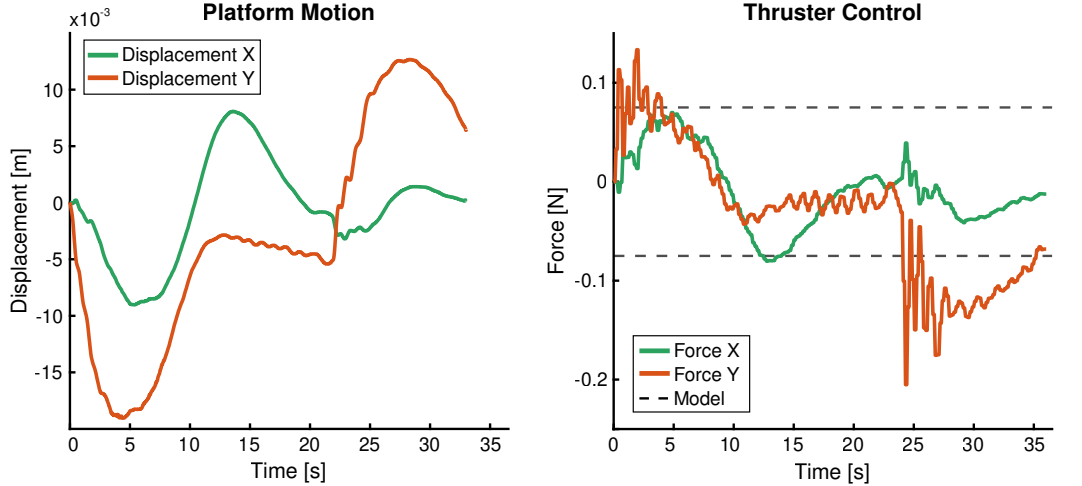
Here we discuss two phenomena to better understand the discrepancies between the model and experimental results of Fig. 6–7. The first is springback, which refers to motion of the feedstock due to the release of residual stresses after plastic deformation [24]. Springback occurs after each bend step during Bend-Forming and affects both the platform
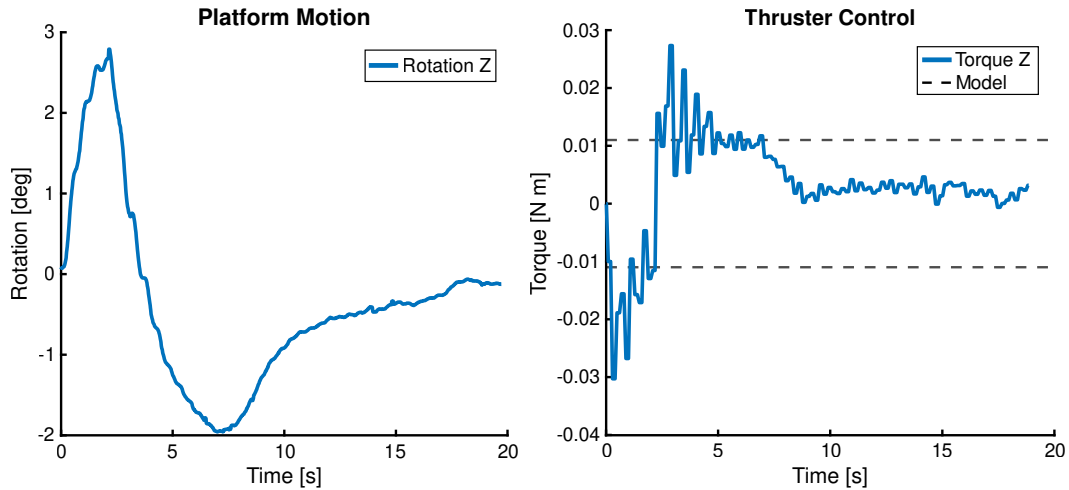
Fig. 5 Snapshots of predicted rigid body motion during free-floating experiments: (a) unit feed of $L = 0.5$ m, (b) unit bend of $\theta = -120°$, (c) zigzag geometry with repeated unit feeds $L = 0.06$ m and unit bends $\theta = \pm90°$.
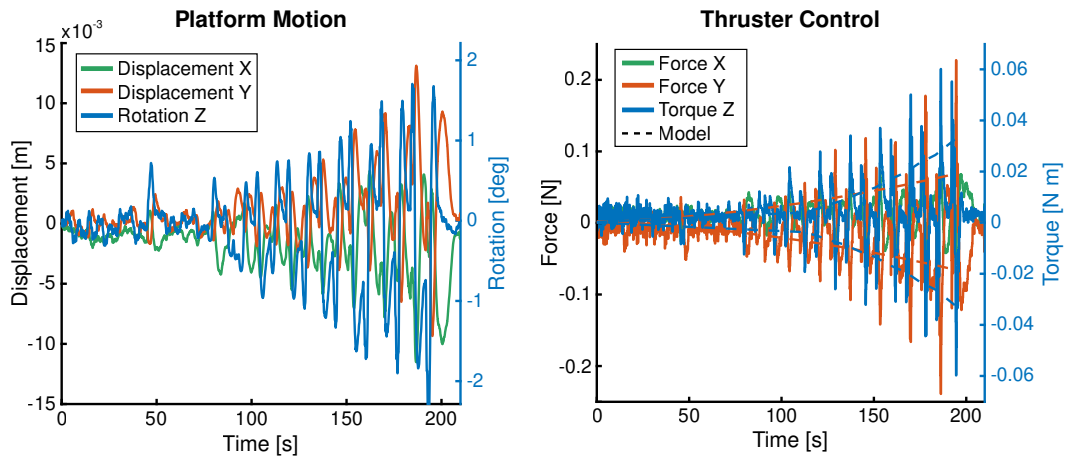
Fig. 6 **Measured motion of the air bearing platform and wire tip during the fabrication sequences of Fig. 5: (a) unit feed of $L = 0.5$ m, (b) unit bend of $\theta = -120°$, (c) zigzag geometry with repeated unit feeds $L = 0.06$ m and unit bends $\theta = \pm 90°$. Dashed lines depict predictions from the rigid body dynamics model.**

Fig. 7 Measured motion of the air bearing platform and commanded forces and torques during the (a) unit feed, (b) unit bend, and (c) zigzag geometry fabrication sequences from Fig. 5 with thruster-based control. Dashed lines show estimates of the maximum control force and torque from the rigid body dynamics model.
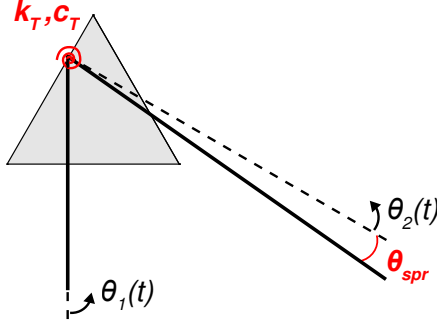
rotation and vibrations of the feedstock. The second phenomenon is control-structure interaction (CSI) [30], which refers to the interaction between the attitude controller and the vibration modes of the system. CSI presents challenges to precise attitude control on spacecraft [31], and here we explore the possibility of CSI during the experiments with closed-loop position and attitude control.

A. Springback Model

The free-floating experimental results (Fig. 6) showed sharp decreases in the platform rotation and oscillations in the wire displacement after each bend step, resulting from the springback of the wire after plastic deformation. To capture this springback effect to first order, we use a 2-DOF model (Fig. 8) with a damped torsional spring at the bend head of the machine. The two degrees of freedom (θ_1, θ_2) model the rotation of the platform and the wire feedstock, respectively, and an initial condition captures the initial springback angle, i.e., $\theta_2(t = 0) = -\theta_{spr}$. Assuming a perfect pivot at the bend head, the equations of motion are

$$\begin{bmatrix} I_1 & 0 \\ 0 & I_2 \end{bmatrix} \begin{bmatrix} \ddot{\theta}_1 \\ \ddot{\theta}_2 \end{bmatrix} + c_T \begin{bmatrix} 1 & -1 \\ -1 & 1 \end{bmatrix} \begin{bmatrix} \dot{\theta}_1 \\ \dot{\theta}_2 \end{bmatrix} + k_T \begin{bmatrix} 1 & -1 \\ -1 & 1 \end{bmatrix} \begin{bmatrix} \theta_1 \\ \theta_2 \end{bmatrix} = \mathbf{0}, \tag{5}$$
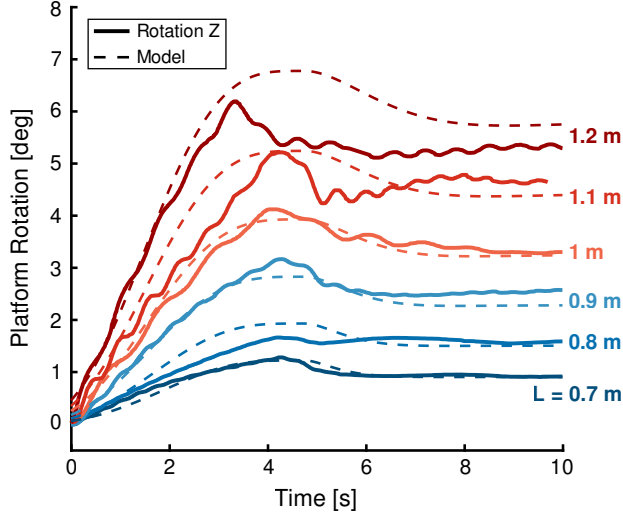
where I_1, I_2 are the mass moments of inertia of the platform and the feedstock about the bend head, respectively, and k_T, c_T are the stiffness and damping coefficients of the torsional spring. This idealized model does not account for deflections of the feedstock nor any energy dissipation due to plastic deformation; it solely aims to capture the platform rotation during springback of the metal feedstock.


Fig. 8   Two degree of freedom (2-DOF) model for springback during Bend-Forming with a torsional spring.

To validate this model, we conducted a series of free-floating experiments with unit bends of $\theta = -120°$ for varying initial wire lengths $L \in [70, 120]$ cm. For comparison, we computed the platform motion using the rigid body dynamics model of Sec. II.B with a larger bend angle of $\theta = -125°$, to account for an approximate springback angle of $\theta_{spr} \approx -5°$. This springback angle and the final platform rotation were then used as initial conditions for the springback model, with a torsional spring stiffness equivalent to the rotational bending stiffness of a cantilever beam, i.e., $k_T = EI/L$ where EI is the bending stiffness of the steel wire.
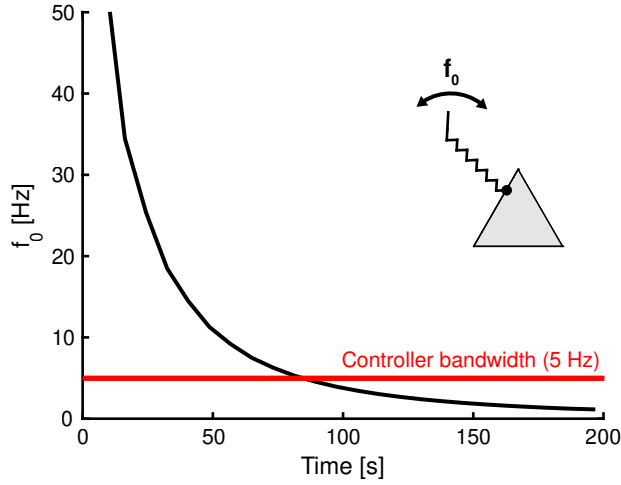
Figure 9 compares the measured platform rotation and the numerical model. A damping coefficient of $c_T = 0.1$ was chosen to yield a reasonable match to the experimental results. The results of Fig. 9 show a decrease in the platform rotation after each bend step, and an increasing effect with increasing initial wire length. The springback model captures this decrease in platform rotation and the increasing effect with initial wire length due to the inverse scaling between the torsional spring stiffness and initial wire length (i.e., $k_T \propto L^{-1}$). With the chosen torsional stiffness and damping coefficients, the model reasonably predicts the measured platform rotation; however, the discrepancy grows with increasing wire length. This is due to deformations of the wire both during and after the plastic deformation which are not considered in the model. A more complete model which accounts for both the wire flexibility and the plastic deformation is needed to capture the full effect of springback. Nonetheless, this analysis highlights the importance of modeling springback in understanding the attitude dynamics during deformation processes like Bend-Forming. For other ISAM processes, other artifacts of the specific construction process such as machine chatter or impulse-induced vibrations may be equally important to model.

Fig. 9 **Measured platform rotation during unit bends of $\theta = -120°$ with varying initial wire lengths L, compared with the combined rigid body dynamics and springback model.**

B. Control-Structure Interaction

The experimental results with thruster control showed that the closed-loop control system was unable to maintain the position and orientation of the platform during the zigzag geometry's longer fabrication sequence (Fig. 7c). Here we consider CSI as a potential cause of this discrepancy. CSI is typically defined as a feedback control instability in which the controller excites the natural modes of the structure and leads to increasing displacements and structural loads [32]. For this reason, a standard practice is to require that the closed-loop ACS bandwidth (in this case, 5 Hz) is at least an order of magnitude below the fundamental natural frequency of the flexible appendage(s) on the spacecraft [30].


Fig. 10 **Fundamental natural frequency of clamped-free zigzag geometry during fabrication. The overlap between the natural frequency and controller bandwidth suggests possible control-structure interaction.**

To assess whether CSI contributed to the increasing error in platform motion during fabrication of the zigzag geometry, we compare the bandwidth of the closed-loop controller used for the experiments (5 Hz) with the natural frequency of the wire structure during fabrication. We estimate this natural frequency in Abaqus by meshing the zigzag geometry after each feed step with linear beam elements (B31) and computing a modal analysis, assuming a clamped node at the bend head and constant material properties of the steel wire ($E = 200$ GPa, $\nu = 0.3$). Figure 10 plots the computed fundamental natural frequency of the zigzag geometry during fabrication, overlaid with the controller

12

bandwidth. This comparison shows that the fundamental natural frequency of the structure decreased below the controller bandwidth at $t \approx 70$ s during the experiment and suggests that CSI was responsible for the increasing error in platform displacement and rotation for $t > 70$ s during the experiment (Fig. 7c). Further experiments are needed to fully assess this effect; nonetheless, this analysis highlights the importance of understanding CSI during ISAM, particularly for large structures whose natural frequencies decrease dramatically during construction.

V. Conclusions and Outlook

This paper has presented experimental and numerical results for the spacecraft attitude dynamics during Bend-Forming, a candidate in-space assembly and manufacturing (ISAM) process for the on-orbit construction of truss structures via plastic deformation of metallic feedstock. Experiments were conducted on a planar air bearing platform to understand the dynamics during fabrication with both free-floating motion and closed-loop, thruster-based attitude and position control. A comparison of the experimental results with a variable-geometry rigid body dynamics model revealed 1) the effect of feedstock springback on the dynamics, and 2) possible control-structure interaction due to the decreasing natural frequency of the structure during fabrication. Future work is needed to better understand how both these phenomena affect attitude control system (ACS) design for ISAM spacecraft. In particular, a key limitation of the present work is in the rigid body modeling of the air bearing platform and wire feedstock. More complete models that account for the wire flexibility and plastic deformation, e.g., with geometrically and materially nonlinear finite elements [33], would better capture the experimental results and provide insights into ACS design. Another limitation is the fabrication of relatively small geometries due to the constraints of the experimental setup and testbed. Ground testing the fabrication of larger truss structures would provide further insights into the effect of mass redistribution on the attitude dynamics and the scaling of ACS requirements with structure size, but requires correspondingly larger experimental facilities.

Even though the experiments conducted in this paper focused on Bend-Forming, the ground testing methodology is equally applicable for understanding the spacecraft attitude dynamics during other candidate ISAM processes. Ground testing will be important for developing robust ACS designs for future ISAM spacecraft, and here we highlight three important guidelines when designing such ground experiments:

- Design experiments to capture the essential physics of the construction steps
- Align experiment goals with testbed constraints
- Minimize interference from external forces and torques

The first guideline is to use ground testing to validate the effects of specific construction steps on the spacecraft attitude dynamics. For deformation processes like Bend-Forming, ground testing revealed that springback is an important consideration to model, and other artifacts may be similarly important to consider for different ISAM processes (e.g. chatter during machining operations, impulse-induced vibrations during joint attachment, etc.). Second, it is important to align the experiment goals with the constraints of the testbed, including the available degrees of freedom, limitations in mass and volume of the fabricated structures, and possible sources of measurement inaccuracy such as platform drift. A third consideration is to minimize interference from external forces and torques, e.g., by implementing active gravity offloading of the fabricated structure. The testing of ultralight deployable structures [19] provides valuable strategies for implementing gravity offloading during ISAM of complex structures. For instance, a cable system that actively follows the structure during the construction process and dynamically adjusts the applied forces [34] is an enabling capability to test the ISAM of larger structures.

With the above guidelines in mind, ground testing can provide valuable insights into spacecraft attitude dynamics during ISAM and inform the ACS design for future ISAM spacecraft. A promising avenue for future research is the design and validation of robust, adaptive controllers that manage the changes in mass properties, the varying environmental disturbance torques, and the risks of CSI on orbit. Designing an attitude control strategy with distributed actuators that are integrated with the ISAM process may offer significant advantages in minimizing the required power consumption and control authority. Additionally, adjusting the fabrication process through input shaping presents an interesting avenue to dampen flexible vibrations during ISAM. Finally, the use of multiple ISAM spacecraft may dramatically reduce the fabrication time of large structures. Ground testing with multiple air bearing platforms would provide insights into multi-spacecraft fabrication.

VI. Acknowledgements

References

[1] Lee, N., Backes, P., Burdick, J., Pellegrino, S., Fuller, C., Hogstrom, K., Kennedy, B., Kim, J., Mukherjee, R., Seubert, C., et al., "Architecture for in-space robotic assembly of a modular space telescope," *Journal of Astronomical Telescopes, Instruments, and Systems*, Vol. 2, No. 4, 2016, pp. 041207–041207. https://doi.org/10.1117/1.JATIS.2.4.041207.

[2] Karumanchi, S., Edelberg, K., Nash, J., Bergh, C., Smith, R., Emanuel, B., Carlton, J., Koehler, J., Kim, J., Mukherjee, R., et al., "Payload-Centric Autonomy for In-Space Robotic Assembly of Modular Space Structures," *Journal of Field Robotics*, Vol. 35, No. 6, 2018, pp. 1005–1021. https://doi.org/10.1002/rob.21792.

[3] Doggett, W., Dorsey, J., Jones, T., Mikulas, M., Teter, J., and Paddock, D., "TriTruss: A New and Novel Structural Concept Enabling Modular Space Telescopes and Space Platforms," *International Astronautical Congress*, 2019. URL https://ntrs.nasa.gov/api/citations/20200010330/downloads/20200010330.pdf.

[4] Suh, J.-E., Dassanayake, S. P., Thomson, M., and Pellegrino, S., "Scalable Concept for Reflector Antenna Assembled in Space," *AIAA Scitech 2024 Forum*, 2024, p. 0823. https://doi.org/10.2514/6.2024-0823.

[5] Kringer, M., Titz, A., Maier, P., Schill, F., Pimpi, J., Hoffman, L., Lafont, U., Reiss, P., and Pietras, M., "Effects of Microgravity and Reduced Atmospheric Pressure on Manufacturing Photopolymer Specimens," *Acta Astronautica*, Vol. 218, 2024, pp. 314–325. https://doi.org/10.1016/j.actaastro.2024.01.033.

[6] "Space Construction Automated Fabrication Experiment Definition Study (SCAFEDS): Final Report, Volume II, Study Results," NASA Contractor Report 160288, 1978. URL https://ntrs.nasa.gov/api/citations/19790021032/downloads/19790021032.pdf.

[7] Levedahl, B., Hoyt, R. P., Silagy, T., Gorges, J., Britton, N., and Slostad, J., "Trusselator™ Technology for In-Situ Fabrication of Solar Array Support Structures," *2018 AIAA Spacecraft Structures Conference*, 2018, p. 2203. https://doi.org/10.2514/6.2018-2203.

[8] Bhundiya, H. G., and Cordero, Z. C., "Bend-Forming: A CNC Deformation Process for Fabricating 3D Wireframe Structures," *Additive Manufacturing Letters*, Vol. 6, 2023, p. 100146. https://doi.org/10.1016/j.addlet.2023.100146.

[9] Hutchinson, L., Imken, T., Farenga, J. C., Solish, B., Matthes, C., and Arthur, P., "Psyche Mission Launch and Solar Array Deployment Phase," *2023 IEEE Aerospace Conference*, IEEE, 2023, pp. 1–13. https://doi.org/10.1109/AERO55745.2023.10115775.

[10] Wilkie, K., and Fernandez, J., "Advanced Composite Solar Sail System (ACS3) Mission Update," *The 6th International Symposium on Space Sailing*, 2023. URL https://ntrs.nasa.gov/citations/20230008378.

[11] Bhundiya, H. G., Marshall, M. A., and Cordero, Z. C., "Fabrication Time Diagrams for In-Space Manufacturing of Large Reticulated Structures," *Journal of Manufacturing Science and Engineering*, Vol. 146, No. 12, 2024, p. 121004. https://doi.org/10.1115/1.4066721.

[12] Spicer, R., and Black, J., "Dynamics Simulation of a Small Satellite with a Robotic Manipulator for Additive Manufacturing," *Journal of Spacecraft and Rockets*, Vol. 61, No. 4, 2024, pp. 975–992. https://doi.org/10.2514/1.A35775.

[13] Zhang, X., Zhu, W., Wu, X., Song, T., Xie, Y., and Zhao, H., "Dynamics and Control for In-Space Assembly Robots with Large Translational and Rotational Maneuvers," *Acta Astronautica*, Vol. 174, 2020, pp. 166–179. https://doi.org/10.1016/j.actaastro.2020.04.063.

[14] Cumer, C., Rognant, M., Biannic, J.-M., and Roos, C., "Modelling and Attitude Control Design for Autonomous In-Orbit Assembly," *ESA GNC 2021*, 2021. URL https://hal.science/hal-03424038/.

[15] Blandino, T., Schroeder, K., Doyle, D., and Black, J., "Attitude Control of an Omni-Directional Aerial Vehicle for Simulating Free-Flyer In-Space Assembly Operations," *AIAA Scitech 2022 Forum*, 2022, p. 0358. https://doi.org/10.2514/6.2022-0358.

[16] Jonckers, D., Tauscher, O., Stoll, E., and Thakur, A., "Feasibility Study of Large-Format, Freeform 3D Printing for On-Orbit Additive Manufacturing," 2021. https://doi.org/10.26153/tsw/17663.

[17] Nakka, Y. K., Foust, R. C., Lupu, E. S., Elliott, D. B., Crowell, I. S., Chung, S.-J., and Hadaegh, F. Y., "A Six Degree-of-Freedom Spacecraft Dynamics Simulator for Formation Control Research," *2018 AAS/AIAA Astrodynamics Specialist Conference*, 2018, pp. 1–20. URL https://authors.library.caltech.edu/records/r1424-xmc64.

[18] Wapman, J. D., Sternberg, D. C., Lo, K., Wang, M., Jones-Wilson, L., and Mohan, S., "Jet Propulsion Laboratory Small Satellite Dynamics Testbed Planar Air-Bearing Propulsion System Characterization," *Journal of Spacecraft and Rockets*, Vol. 58, No. 4, 2021, pp. 954–971. https://doi.org/10.2514/1.A34857.

[19] Banik, J. A., and Jenkins, C. H., *Testing Large Ultra-Lightweight Spacecraft*, American Institute of Aeronautics and Astronautics, Inc., 2017. https://doi.org/10.2514/4.104657.

[20] Few, A., Lockett, T., Wilson, R., and Boling, D., "Testing and Development of NEA Scout Solar Sail Deployer Mechanism," *Aerospace Mechanisms Symposium*, 2018. URL https://ntrs.nasa.gov/api/citations/20180005158/downloads/20180005158.pdf.

[21] Cheng, W., Kee, C., and Wirzburger, J., "Parker Solar Probe MAG Boom Design, Analysis and Verification," *Proceedings of the 45th Aerospace Mechanisms Symposium, NASA Johnson Space Center*, 2020. URL https://www.esmats.eu/amspapers/pastpapers/pdfs/2020/cheng.pdf.

[22] Sternberg, D. C., Pong, C., Filipe, N., Mohan, S., Johnson, S., and Jones-Wilson, L., "Jet Propulsion Laboratory Small Satellite Dynamics Testbed Simulation: On-Orbit Performance Model Validation," *Journal of Spacecraft and Rockets*, Vol. 55, No. 2, 2018, pp. 322–334. https://doi.org/10.2514/1.A33806.

[23] Rivera, K. D., Sternberg, D., Lo, K., and Mohan, S., "Multi-Platform Small Satellite Dynamics Testbed," *2023 IEEE Aerospace Conference*, IEEE, 2023, pp. 1–7. https://doi.org/10.1109/AERO55745.2023.10116022.

[24] Eggertsen, P.-A., and Mattiasson, K., "On the Modelling of the Bending–Unbending Behaviour for Accurate Springback Predictions," *International Journal of Mechanical Sciences*, Vol. 51, No. 7, 2009, pp. 547–563. https://doi.org/10.1016/j.ijmecsci.2009.05.007.

[25] Quadrelli, M. B., Cameron, J. M., and Balaram, B., "Modeling and Simulation of Flight Dynamics of Supersonic Inflatable Advanced Decelerator," *AIAA/AAS Astrodynamics Specialist Conference*, 2014, p. 4454. https://doi.org/10.2514/6.2014-4454.

[26] Eke, F. O., "Dynamics of Variable Mass Systems," University of California Davis, Davis, CA, Mar. 1998. NASA Report 208246, URL https://ntrs.nasa.gov/api/citations/19980210404/downloads/19980210404.pdf.

[27] Marshall, M. A., and Pellegrino, S., "Slew Maneuver Constraints for Agile Flexible Spacecraft," *Journal of Guidance, Control, and Dynamics*, Vol. 46, No. 12, 2023, pp. 2300–2314. https://doi.org/10.2514/1.G007430.

[28] Sola, J., "Quaternion Kinematics for the Error-State Kalman Filter," 2017. URL https://hal.science/hal-01122406v3.

[29] Géradin, M., and Cardona, A., *Flexible Multibody Dynamics: A Finite Element Approach*, John Wiley and Sons, 2001.

[30] Spanos, J. T., "Control-Structure Interaction in Precision Pointing Servo Loops," *Journal of Guidance, Control, and Dynamics*, Vol. 12, No. 2, 1989, pp. 256–263. https://doi.org/10.2514/3.20399.

[31] Sackett, L., and Kirchwey, C., "Flight Control, Dynamics, and Structural Interaction on the Space Shuttle Hubble Space Telescope Servicing Mission," *Astrodynamics Conference*, 1994, p. 3748. https://doi.org/10.2514/6.1994-3748.

[32] Bedrossian, N., "International Space Station Assembly and Operation Control Challenges," *AAS Guidance and Control Conference*, Citeseer, 2000. URL https://citeseerx.ist.psu.edu/document?repid=rep1&type=pdf&doi=84826bfdc2413b0d7e7be9126ac7dac42a743a6a#page=23.

[33] Belytschko, T., Liu, W. K., Moran, B., and Elkhodary, K., *Nonlinear Finite Elements for Continua and Structures*, John Wiley and Sons, 2014.

[34] Sullivan, C., Gebhardt, K., Solis, C., Mitchell, T., and Pehrson, N. A., "Accurate Microgravity Simulation for Deployable Structures," *AIAA Scitech 2023 Forum*, 2023, p. 1885. https://doi.org/10.2514/6.2023-1885.